Patterns of Precipitation Change and Climatological Uncertainty among CMIP5 Models, with a Focus on the Midlatitude Pacific Storm Track*

Baird Langenbrunner and J. David Neelin

Department of Atmospheric and Oceanic Sciences, University of California, Los Angeles, Los Angeles, California

Benjamin R. Lintner

Department of Environmental Sciences, Rutgers, The State University of New Jersey, New Brunswick, New Jersey

Bruce T. Anderson

Department of Earth and Environment, Boston University, Boston, Massachusetts

(Manuscript received 25 November 2014, in final form 17 July 2015)

ABSTRACT

Projections of modeled precipitation (P) change in global warming scenarios demonstrate marked intermodel disagreement at regional scales. Empirical orthogonal functions (EOFs) and maximum covariance analysis (MCA) are used to diagnose spatial patterns of disagreement in the simulated climatology and end-of-century P changes in phase 5 of the Coupled Model Intercomparison Project (CMIP5) archive. The term principal uncertainty pattern (PUP) is used for any robust mode calculated when applying these techniques to a multimodel ensemble. For selected domains in the tropics, leading PUPs highlight features at the margins of convection zones and in the Pacific cold tongue. The midlatitude Pacific storm track is emphasized given its relevance to wintertime P projections over western North America. The first storm-track PUP identifies a sensitive region of disagreement in P increases over the eastern midlatitude Pacific where the storm track terminates, related to uncertainty in an eastward extension of the climatological jet. The second PUP portrays uncertainty in a zonally asymmetric meridional shift of storm-track P, related to uncertainty in the extent of a poleward jet shift in the western Pacific. Both modes appear to arise primarily from intermodel differences in the response to radiative forcing, distinct from sampling of internal variability. The leading storm-track PUPs for P and zonal wind change exhibit similarities to the leading uncertainty patterns for the historical climatology, indicating important and parallel sensitivities in the eastern Pacific storm-track terminus region. However, expansion coefficients for climatological uncertainties tend to be weakly correlated with those for end-of-century change.

1. Introduction

Accurate prediction of end-of-century precipitation (P) change as a result of global warming is critical to the assessment of future changes in the hydrological cycle, especially at regional scales relevant to water resource management and decision-making. Global climate models (GCMs) run as part of phases 3 and 5 of the Coupled Model Intercomparison Project (CMIP3 and CMIP5; Meehl et al. 2007; Taylor et al. 2012) exhibit robust agreement over large-scale changes related to thermodynamic arguments that regions of climatological moisture convergence will get wetter (the tropics and middle-to-high latitudes), while regions of climatological moisture divergence will get drier (the subtropics). This concept was first noted by Manabe and Stouffer (1980) and Manabe and Wetherald (1980) and is now referred to as the wet-get-wetter or rich-get-richer mechanism (Chou and Neelin 2004; Held and Soden 2006; Trenberth 2011). It has been documented extensively in the CMIP archives, and the patterns it describes can be seen in individual models as well as in
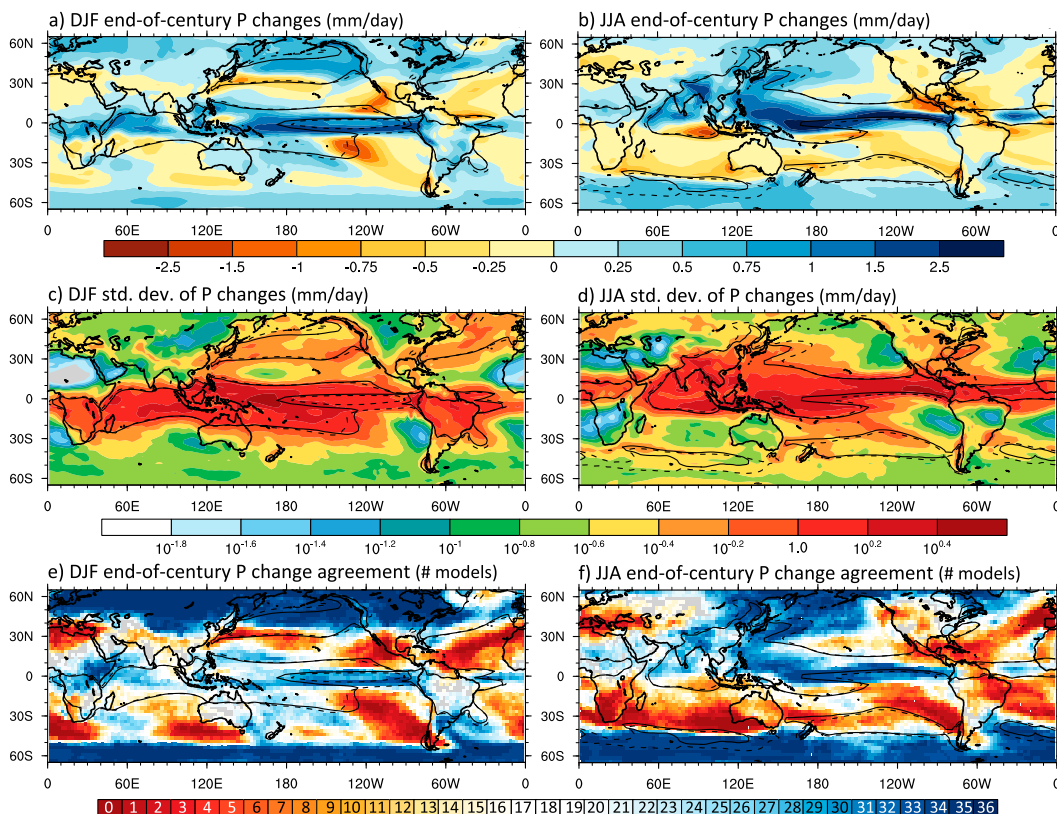
FIG. 1. The 36-member MME mean end-of-century P changes for the (a) DJF and (b) JJA seasons. Anomalies are calculated for the 2070–2100 climatology relative to a 1960–90 base period. Standard deviation of P anomalies across the 36-model ensemble for the (c) DJF and (d) JJA seasons. (e),(f) Agreement on positive P anomalies for the same models and seasons. In all maps, solid (dashed) lines represent the 1960–90 (2070–2100) 4 mm day^{-1} P climatology.

the multimodel ensemble (MME) mean of projected P changes (see Figs. 1a,b). Recent studies have noted that these changes are detectable in ocean observations (Durack et al. 2012), but their validity can break down at the regional or gridpoint level (Chadwick et al. 2013; Roderick et al. 2014), especially for changes over land (Greve et al. 2014). Alongside these thermodynamic changes are notable dynamic changes in the atmospheric circulation that ultimately affect P projections, typically framed in terms of a poleward expansion of subtropical dry zones or the descending branch of the Hadley cell, as well as a poleward shift, upward expansion, and slight widening of the climatological storm track (Yin 2005; Lu et al. 2007; Seager and Vecchi 2010; Scheff and Frierson 2012b,a; Chang et al. 2012; see Figs. 1a,b).

Outside of a large-scale or mean meridional framework, however, intermodel agreement on P changes can diminish greatly. The standard deviation of gridpoint (local) P changes across models is one way of quantifying this spread (see Figs. 1c,d), and complex P changes occurring in the tropics or along convective margins can

lead to large disagreement in tropical P projections (Neelin et al. 2003; Chou and Neelin 2004; Chou et al. 2009), especially over land (e.g., Yin et al. 2013), even when models agree on bulk measures of tropical change, such as distributions of precipitation intensity (Lintner et al. 2012). Substantial regional uncertainty also exists in areas with large internal variability in the P climatology, leading to small signal-to-noise ratios in future projections and to noticeable uncertainty and conflicting model changes (Giorgi and Francisco 2000; Allen and Ingram 2002; Neelin et al. 2006; Tebaldi and Knutti 2007; Hawkins and Sutton 2011; Tebaldi et al. 2011; Deser et al. 2012; Mahlstein et al. 2012; Knutti and Sedlácek 2013; Roderick et al. 2014). These regions are often located between P increases at middle-to-high latitudes and decreases in the subtropics, where thermodynamic arguments become less dominant and projections are susceptible to disagreement in dynamic feedbacks at regional scales (Chou et al. 2009; Seager and Vecchi 2010; Shepherd 2014).

In addition to uncertainty in P projections, models exhibit a range of abilities in simulating historical P

climatology and internal variability in CMIP3 and CMIP5 (Deser et al. 2012; Flato et al. 2013). This is especially true for the tropics, where considerable ocean–atmosphere feedbacks, as well as differences in model parameterization of deep convection, can cause discrepancies in the P climatology (e.g., Mechoso et al. 1995; Zhang 2001; Lin 2007; Brown et al. 2013) and projected changes (Collins et al. 2011; Brown et al. 2012) among models. GCM biases also exist outside of the tropics, especially at regional scales where local dynamics come into play (e.g., Kumar et al. 2013; Langford et al. 2014; Mehran et al. 2014). Finally, only modest (if any) improvement has been found between CMIP3 and CMIP5 in these biases or in constraining regional model disagreement in end-of-century changes (Knutti and Sedláček 2013; Sheffield et al. 2013a,b; Maloney et al. 2014; Hirota and Takayabu 2013).

One region that is particularly sensitive to P change uncertainty is the North American west coast between the latitudes of approximately 30° and 50°N. This area lies at the eastern terminus of the Pacific wintertime storm track and is situated between robust P decreases at lower latitudes and increases at higher latitudes (Neelin et al. 2013; Berg et al. 2015; Seager et al. 2014). In this region, P exhibits substantial variability on interannual to interdecadal time scales—especially in the North American southwest and in southern California (Dettinger et al. 1998)—so that in future projections, signal-to-noise ratios tend to be small and dynamical changes complex (Seager and Vecchi 2010; Seager et al. 2014). Studies have also noted GCM uncertainty in simulating the climatological Pacific storm track feeding into this region (Delcambre et al. 2013a), as well as widespread disagreement in end-of-century storm-track changes (Yin 2005; Bengtsson et al. 2006; Ulbrich et al. 2008; Ihara and Kushnir 2009; Chang et al. 2012; Chang 2013; Delcambre et al. 2013b; Grise and Polvani 2014; Simpson et al. 2014).

In this paper, we visualize intermodel uncertainty patterns for P projections and climatologies in the CMIP5 ensemble, and we seek coupled or associated patterns of uncertainty in circulation and temperature fields. We do this by applying empirical mode decomposition techniques—commonly used in the space–time domain—to the "space-model index" domain. In the latter half of our analysis, we emphasize the wintertime midlatitude Pacific storm track region, and in doing so we illustrate the benefits of cross checking with complementary methods and show that using several in tandem can strengthen the conclusions drawn for each.

The rest of this study is laid out as follows: section 2 discusses data and methods. Section 3 reviews end-of-century P changes in the CMIP5 ensemble. Section 4

shows selected regional disagreement patterns, and sections 5–7 focus on the wintertime Pacific storm-track region. Section 8 contains our summary and conclusions. Supplemental information is also available for download and is discussed in this manuscript.

2. Data, methods, and terminology

a. CMIP5 data

The primary ensemble in our analysis consists of 36 fully coupled GCMs; historical forcing and representative concentration pathway 8.5 (RCP8.5) simulations were used for each model. An additional ensemble of 30 atmosphere-only runs was also used. Table S1 in the supplemental material lists model information for both ensembles. In some cases, additional ensemble members for a given coupled model were used in order to estimate internal variability; for these models, the total number of additional realizations is included in the second column of Table S1.

We downloaded the following fields, all at monthly resolution: P, zonal (U) and meridional (V) winds at 200 hPa (U200 and V200) and 850 hPa (U850 and V850), surface air temperature (TAS), and skin temperature (TS). We treat the models in each ensemble as independent samples, though we acknowledge that some of them share structural cores and may have common biases (Jun et al. 2008b,a; Knutti et al. 2010, 2013). Our goal is to understand intermodel uncertainty relative to the MME mean, not to the "true climate" or observations.

Seasonal end-of-century changes for the RCP8.5 scenario were calculated for each model by differencing the climatology at the end of the twenty-first century (2070–2100) and over a twentieth-century base period (1960–90). The historical climatologies of the atmosphere-only models cover 1979–2009. The 30-yr averages were chosen to minimize interannual-to-decadal model variability; all fields were regridded via bilinear interpolation to a common 2.5° × 2.5° grid prior to analysis.

b. Methods

The methods are described in more detail in the supplemental information, though a brief summary is provided here, taking P as the example variable.

We use EOF analysis to visualize spatial patterns of model uncertainty in end-of-century P changes. These EOFs are calculated across the model dimension—as opposed to the conventional time dimension—and the resulting modes show patterns of intermodel disagreement over end-of-century P changes relative to the MME mean. Gridpoint correlation maps between

expansion coefficients of *P* change uncertainty patterns and temperature or winds allow one to find associated uncertainties in other variables. We also use maximum covariance analysis [MCA; sometimes referred to as singular value decomposition (SVD)]. MCA is performed on the covariance matrix between two variables (e.g., *P* changes and U200 changes), producing pairs of uncertainty patterns that represent coupled ensemble disagreement.

Our methods complement other studies that have used similar methods to examine uncertainty patterns in GCMs, including intermodel disagreement in tropical *P* change and its connection to SST uncertainties (Li and Xie 2012; Ma and Xie 2013; Li and Xie 2014), GCM skill in modeling historical midlatitude jets, uncertainty in jet changes, and relationships with tropical SST uncertainties (Delcambre et al. 2013a,b), and relationships between large-scale SST uncertainties and global warming trends in land surface *P* (Anderson et al. 2015). Similar methods have also been used in the weather forecasting community for medium-range ensemble forecasts (e.g., Harr et al. 2008; Keller et al. 2011; Zheng et al. 2013; Chang and Zheng 2013).

c. Principal uncertainty pattern terminology

For brevity, we refer to all modes that arise from the matrix decomposition techniques described above as principal uncertainty patterns (PUPs), and we use this term interchangeably with patterns or modes from the EOF and MCA analyses when discussing results. This is done to emphasize that these techniques all seek to capture robust patterns of uncertainty common among models in an ensemble, even though the methodology used to calculate each may differ.

3. End-of-century *P* changes in the CMIP5 ensemble

To lay the basis for our discussion, Figs. 1a,b show the MME mean global end-of-century *P* change in the RCP8.5 scenario, for the December–February (DJF) and June–August (JJA) seasons. Seasonal 4 mm day^{-1} contours for the base (solid) and future (dashed) periods are shown for the MME mean to establish approximate geographical boundaries for regions of deep convection and storm-track precipitation.

Localized standard deviation plots (Figs. 1c,d) give a sense of how individual model *P* changes spread about the MME mean. In both seasons, the largest spread is over the oceans and within tropical zones of deep convection, implicating intermodel uncertainty in changes occurring to moisture fluxes and deep convective processes in these regions. In DJF (Fig. 1c), the largest

intermodel spread is over the western Pacific warm pool and South Pacific convergence zone (SPCZ). Secondary regions include the cold tongue region off the coast of Peru and Ecuador, the Atlantic ITCZ, and the Indian Ocean. In JJA (Fig. 1d), the western and eastern Pacific are still major areas of spread, as are the tropical Indian and Atlantic Oceans and the Asian monsoon region. Note these hotspots of disagreement do not always coincide with areas of largest absolute *P* change (Figs. 1a,b) or *P* change as a percent of the historical climatology (see Figs. S1a,b in the supplemental material).

We also show agreement plots on the sign of *P* changes (Figs. 1e,f; plotted for agreement on positive change). Relative to the standard deviation maps, the white regions in agreement maps reach wider into the extratropics and midlatitudes, where intermodel spread is a result of changes to both regional dynamics and local thermodynamics. Our concern here is *P* change disagreement at regional scales (i.e., at the scale of climate features such as convection zones or storm tracks), though an equivalent global analysis is shown in the supplemental information for absolute *P* changes (see Figs. S2 and S3 in the supplemental material) and *P* change as a percent of the base period climatology (see Figs. S4 and S5 in the supplemental material). These patterns show tropical dominance in intermodel disagreement, even with normalization by the climatology, and so we turn to a regional PUP analysis.

4. Regional PUPs of *P* change disagreement

a. Criteria for selecting regional PUP domains

We select regional domains using the following criteria: 1) if the regional PUPs are to have any significance, there should be sizeable disagreement in the region of interest; 2) objective pattern-seeking techniques are sensitive to the domain size and characteristics, and edge effects can arise as domain boundaries change; and 3) seasonality comes into play when spatial disagreement patterns are the objective, since zones of heavy *P* and storm-track domains will shift seasonally, and it is important not to segment climatological features.

b. Regional PUPs using EOF analysis

For DJF, we produce *P* change PUPs for the following regions: the Indian Ocean, the tropical Pacific, the North Pacific storm-track region, and equatorial South America. For JJA, the regions include the following: the Asian monsoon region, the central and western tropical Pacific, the South Pacific storm-track region, Central America (encompassing the eastern tropical Pacific), and the
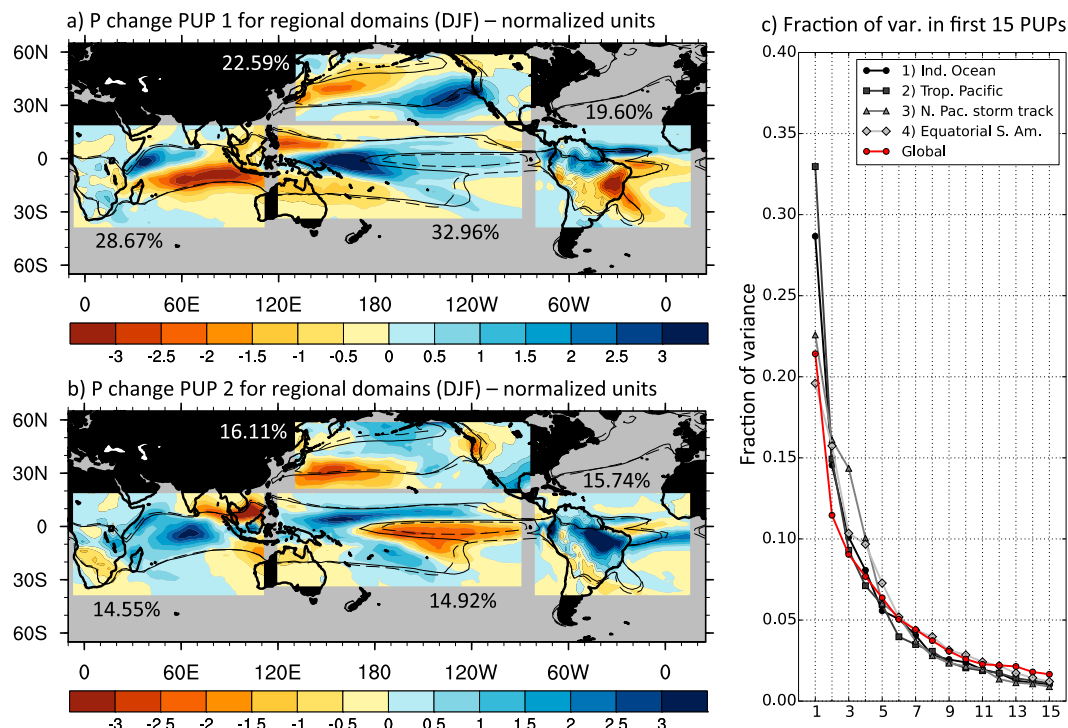
FIG. 2. (a) First and (b) second PUPs for the regions shown in DJF. From left to right, the regions are the Indian Ocean, the tropical Pacific, the North Pacific storm track, and equatorial South America. For each mode and region, the variance of intermodel disagreement that the PUP accounts for is shown as a percent. (c) The fraction of variance accounted for in each region for the first 15 modes. Tropical regions show a much stronger response when *P* units are used, so to plot patterns on a common graph, each region has been normalized by the spatial standard deviation of its EOF values; a unit of ±1 therefore represents a "standard departure" from the MME mean in that region. More detail on these regions and units can be found in Table 1.

equatorial Atlantic region. This regional analysis reveals second-order and structural characteristics that are not revealed in simpler analyses like those in Figs. 1c–f.

The first two EOF PUPs for these domains are shown in Figs. 2 (DJF) and 3 (JJA). To plot PUPs on a common graph, each mode is normalized by its spatial standard deviation. Figures 2c and 3c show the percent variance that successive modes account for in the EOF analyses (cut off after 15 modes). For DJF, two regions of uncertainty include the southern edge of the Indian Ocean convection zone and the tropical Pacific at the western edge of the cold tongue. For JJA, one can see uncertainty along the southern edge of the ITCZ and along the northern edge of the cold tongue region in the tropical Pacific.

Table 1 lists details about normalization, latitude, and longitude range of the domains, and the percent variances accounted for by the displayed modes. Leading regional PUPs tend to explain 20%–30% of intermodel uncertainty, and features commonly occur on edges of convection zones, within storm tracks, and over the equatorial cold tongue. We also include the correlation coefficient between expansion coefficients for the

regional and global domains [r(reg, glob)], noting that in some cases PUPs can change order (or be spread across several modes). These correlations tend to be higher for the tropical domains in Figs. 2 and 3, reinforcing the dominance of the tropics in global-scale uncertainty, although there are also notable correlations at higher latitudes.

We focus on the DJF midlatitude Pacific storm-track region for the remainder of this study. We chose the Pacific storm-track region after noting strong separation and clear signals in the first two PUPs (see Figs. 2a,b for the modes in this domain, as well as Fig. 2c to get a sense of mode separation).

5. Uncertainty in *P* change in the midlatitude Pacific storm-track domain

a. Storm-track P change PUPs and associated uncertainties in circulation changes

In the midlatitude Pacific, the wintertime storm track is a preferred region of cyclone activity, generated by baroclinic instability and acting to transport momentum,
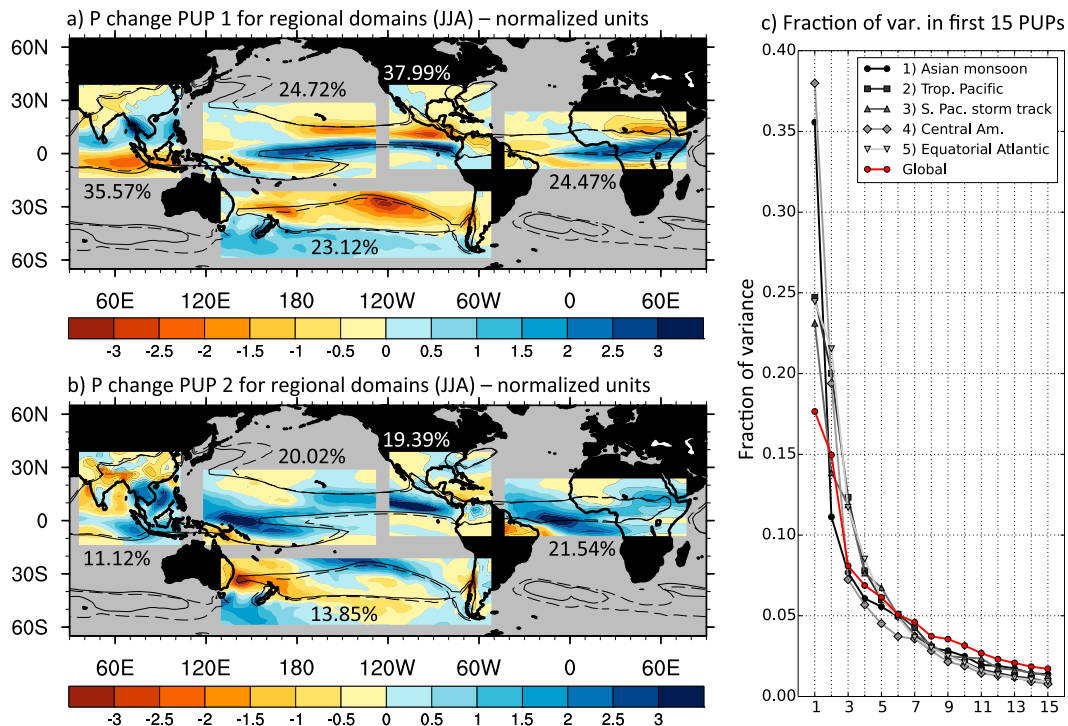
FIG. 3. As in Fig. 2, but for the JJA season. From left to right, the regions are the Asian monsoon, the tropical Pacific, the South Pacific storm track, Central America, and the equatorial Atlantic. The variance fraction accounted for by that mode is included next to each region as in Fig. 2. (c) The fraction of variance accounted for in each region for the first 15 modes. The regions and units for PUP patterns are discussed in Table 1.

heat, and moisture poleward. We use the $4\,\mathrm{mm\,day}^{-1}$ contour as an approximate storm-track outline in the base and future periods. Cyclones that produce precipitation in this region are steered by the upper-level jet across the Pacific and trail into the North American west coast, and so we inspect uncertainties in P change in the context of the broader upper- and lower-level circulation. Delcambre et al. (2013a,b) have extensively documented uncertainties in the jet for this region, and we will discuss model disagreement in a similar way by highlighting the two leading modes:

1) The "jet extension" mode describes disagreement in the eastward extension of the jet and resulting P changes at the eastern terminus of the storm track, where the $4\,\mathrm{mm\,day}^{-1}$ contour hooks slightly northeast at approximately 35°N, 140°W.

2) The "meridional shift" mode describes uncertainty in the extent of a meridional shift or poleward displacement of the storm track P, with increases on the poleward edge and decreases on the equatorward edge of the $4\,\mathrm{mm\,day}^{-1}$ contour (see Figs. 1a,c).

Figure 4 shows the first (Figs. 4a,c) and second (Figs. 4b,d) PUPs of the EOF analysis on P changes in the storm track region (replotted from Figs. 2a,b but

with units of millimeter per day). Vectors representing coupled disagreement in upper- and lower-level wind changes are overlaid, the components of which are regressions of end-of-century U and V changes onto the expansion coefficients for each mode.

We identify the first PUP (Figs. 4a,c) as a jet extension mode, with an east–west dipole showing P increases on the southeast flank of the storm track as well as decreases over the western Pacific. The wind vectors form a cyclonic circulation pattern slightly to the northwest of this center at both upper (Fig. 4a) and lower (Fig. 4c) levels, implying that to a first approximation this pattern represents an equivalent barotropic mode of disagreement.

We identify the second PUP (Figs. 4b,d) as a meridional shift mode, showing drying along the equatorward edge of the storm track in the western half of the domain and implying disagreement among models in the location and magnitude of poleward P shifts in this region. Upper-level wind regressions (Fig. 4b) show associated anticyclonic uncertainties in circulation along the equatorward edge of the storm track.

We use the terminology extension and shift to give names to the uncertainty patterns, though the changes occurring to the midlatitude jet and resulting P in the

TABLE 1. Details for the regional PUP analysis shown in Figs. 2 and 3. For the first two regional modes, we list the percent variance accounted for in that mode (column 2), the correlation coefficient between the expansion coefficients for that mode and the expansion coefficients for the corresponding global modes 1 and 2 (columns 3 and 4), and the spatial standard deviation (σ) of the EOF in that domain (column 5, used for normalizing patterns in Figs. 2 and 3). Because the sign of any EOF mode is arbitrary, we show the absolute value of the correlation coefficient. Correlations are in boldface where they pass a two-tailed Student's t test at the 95% confidence level.

	Regional mode	Variance (%)	$|r(\mathrm{reg, glob1})|$	$|r(\mathrm{reg, glob2})|$	σ (mm day^{-1})
Region (DJF)					
Indian Ocean	1	28.67	**0.57**	**0.71**	0.44
40°S–20°N, 10°–120°E	2	14.55	**0.53**	0.31	0.32
Tropical Pacific	1	32.96	**0.98**	0.16	0.70
35°S–20°N, 125°E–95°W	2	14.92	0.03	**0.53**	0.47
North Pacific storm track	1	22.59	0.03	0.12	0.21
20°S–60°N, 135°E–90°W	2	16.11	**0.45**	**0.61**	0.18
Equatorial South America	1	19.60	0.14	**0.80**	0.32
40°S–20°N, 90°W–5°E	2	15.74	0.11	**0.35**	0.27
Region (JJA)					
Asian monsoon	1	35.57	**0.94**	0.10	0.76
15°S–40°N, 65°–125°E	2	11.12	0.04	**0.62**	0.42
Tropical Pacific	1	24.72	0.31	**0.78**	0.67
15°S–30°N, 135°E–125°W	2	20.02	**0.83**	0.33	0.54
South Pacific storm track	1	23.12	0.06	0.06	0.18
60°S–20°N, 145°E–60°W	2	13.85	**0.58**	0.17	0.14
Central America	1	37.99	0.08	**0.91**	0.71
10°S–40°N, 120°W–60°W	2	19.39	**0.75**	0.03	0.50
Equatorial Atlantic	1	24.47	0.25	**0.80**	0.73
10°S–25°N, 55°W–40°E	2	21.54	**0.86**	0.30	0.57

midlatitude Pacific are asymmetric and complex. One robust feature found in the CMIP5 archive is a poleward jet shift in the western Pacific but an equatorward shift in the east (Simpson et al. 2014; Park and An 2014). Simpson et al. (2014) attribute this equatorward shift in the eastern Pacific to a barotropic stationary wave anomaly off the west coast of North America. Neelin et al. (2013) investigated the CMIP5 MME mean P changes occurring in this region, noting a slight but statistically significant increase in the region where the climatological storm track approaches the California coast, between approximately 33° and 42°N. Seager et al. (2014) attributed this increase primarily to enhanced mean flow moisture convergence. The circulation regressions in Figs. 4a,b may reflect model uncertainty in changes to the mean circulation (and associated stationary wave patterns), which would feed into uncertainty in P change in the storm-track termination region.

The first and second U200 change PUPs are displayed in Figs. 4e,f. Note that the first mode (Fig. 4e) reinforces the jet extension interpretation: models exhibit disagreement in U200 increases in the jet core, providing a source of uncertainty in the extent to which storms are steered onto the North American west coast. The second mode (Fig. 4f) seems to suggest intermodel spread over the extent of a poleward shift of the jet in the western Pacific. However, it is actually the third mode

for U200 changes (not shown) that is more strongly related to the meridional shift P change PUP (see supplemental information for details). To better see coupled uncertainties between jet and P change uncertainty, we show MCA results in section 6.

b. Internal variability versus intermodel uncertainty

To get a sense of how individual models contribute to the uncertainty patterns in Fig. 4, expansion coefficients for P change PUPs are shown in Figs. 5a,b. Red dots represent expansion coefficients for each of the 36 models in the ensemble and characterize total ensemble spread (i.e., a combination of internal variability, climatological uncertainty, and intermodel differences in the response to radiative forcing). The MME mean is represented by the zero line, and the box-and-whisker plots to the right show the overall spread of models about the mean (see caption for details). For models with additional ensemble runs available, black dots show the projection of those P changes onto the PUPs in Figs. 4a–d. The relative spread of the black and red dots indicates that internal model variability is small compared to overall intermodel uncertainty.

We also estimate internal variability using preindustrial control (piControl) runs, which vary in length from 240 to 1050 years in the models. We calculate the DJF P climatology for nonoverlapping 30-yr periods and produce N_{30} climatologies for each model (see Table S1
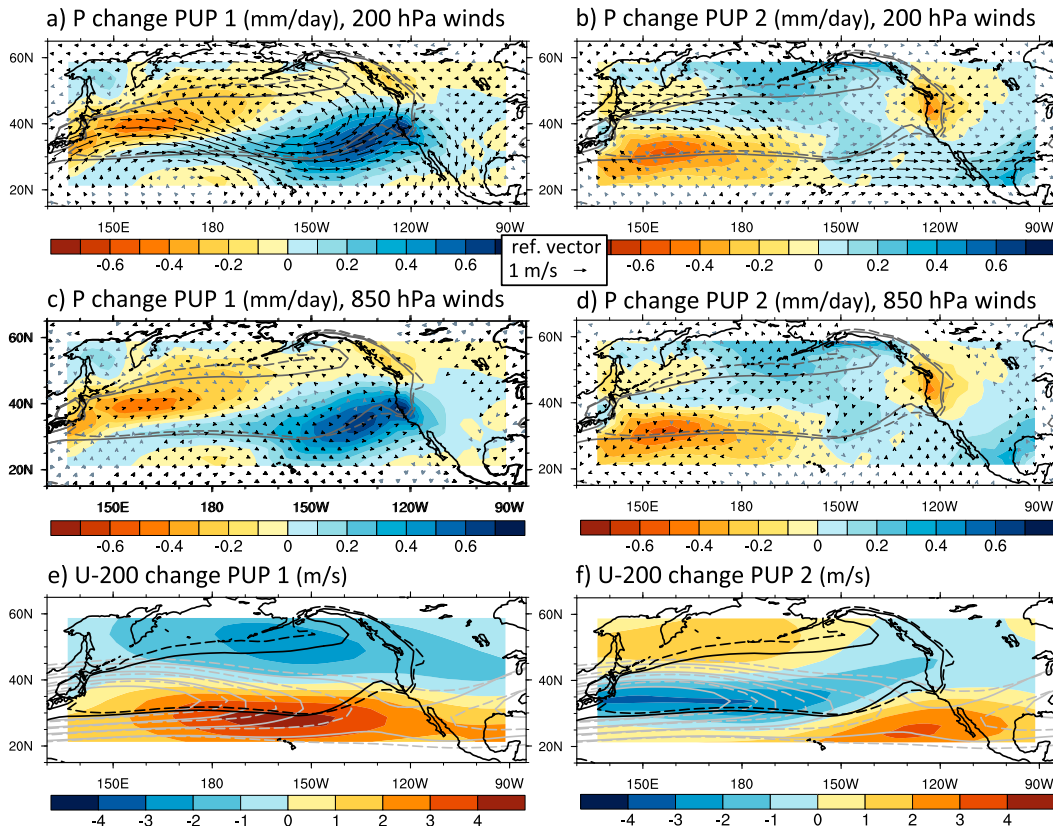
FIG. 4. First and second *P* change PUPs for the midlatitude Pacific storm-track region during DJF. The *P* change PUPs (a) 1 and (b) 2 (shading) with 200-hPa *U* and *V* change regressions. (c),(d) As in (a),(b) but for winds at 850 hPa. Black solid and dotted contours are as in Fig. 1. Wind vectors are drawn in proportion to the 1 m s^{-1} reference vector. Vectors are plotted black where at least one component passes a two-tailed Student's *t* test at the 90% confidence level, and gray otherwise. (e) First and (f) second EOF U200 change PUPs during DJF. Gray solid contours show isotachs for the base period MME mean, and dashed contours show isotachs for the end-of-century MME mean, starting at 30 m s^{-1} and plotted at intervals of 10 m s^{-1}. The first *P* change PUP accounts for 22.59% of intermodel variance in *P* change projections, and the second *P* change PUP accounts for an additional 16.11%. The first U200 change PUP accounts for 41.80% of intermodel variance, and the second mode accounts for an additional 23.13%.

in the supplemental material for details). We center these climatologies by that model's long-term mean at each grid point and then take all possible pairwise combinations without repeat. The difference between each pair is taken, and the result is projected onto the *P* change PUPs in Figs. 4a–d. The resulting values represent expansion coefficients for internal variability. The error bars in Figs. 5a,b show plus and minus one standard deviation of these values for each model, centered at zero on the *y* axis, representing the spread that can be attributed to internal *P* variability alone in the storm-track region. This tests whether the intermodel spread seen by the red dots in Figs. 5a,b could arise solely from internal variability. The magnitude of these error bars is a modest fraction of the ensemble spread, providing evidence that to leading order, intermodel differences in the response to radiative forcing are likely driving

much of the spread captured by these uncertainty patterns, and internal variability does not contribute substantially. We explore the role of interannual SST variability and, in particular, ENSO forcing in the next section.

c. Extension and shift modes from MCA

MCA helps reveal coupled patterns in *P* and U200 change uncertainties that are seen qualitatively in Fig. 4. In Fig. 6, we show MCA results for coupled *P* and U200 change PUPs, along with diagrammatic arrows to illustrate the extension and shift modes. Figures 6a,c show the first coupled mode patterns; an arrow in Fig. 6a shows location of strong *P* change disagreement in the storm-track termination region, and an identical arrow in Fig. 6c shows collocated model uncertainty in U200 increases in the historical jet core. Figures 6b,d show the
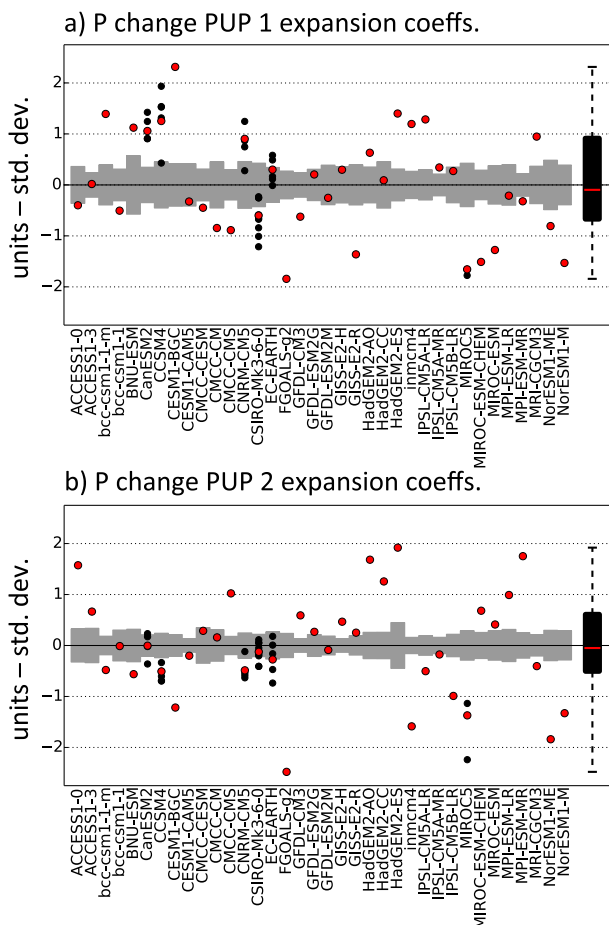
a) P change PUP 1 expansion coeffs.

b) P change PUP 2 expansion coeffs.

FIG. 5. Expansion coefficients for the (a) first and (b) second *P* change PUPs. Red dots represent each of the 36 models in the ensemble. Black dots show expansion coefficients for additional ensemble members (see text and Table S1 in the supplemental material for details). Error bars show internal variability estimation using preindustrial control runs in the models (see text for details).

second coupled mode patterns; the arrow in Fig. 6b depicts intermodel disagreement in the poleward displacement of the storm track in the western half of the domain, and the arrow in Fig. 6d shows associated disagreement where the U200 jet is displaced from its historical maximum. MCA here becomes a useful tool for isolating coupled patterns of uncertainty in *P* and U200 change uncertainties that are not obvious in the separate EOF analyses.

Last, we have tested the patterns in this storm-track region and note they are not sensitive to domain size, in that changing the domain boundaries by a few degrees latitude or longitude causes the fraction accounted for by individual modes to change only within a few percent, and the appearance and qualitative details of the PUPs themselves are stable.

6. Multivariate PUPs for *P* and surface temperature

Figures 7a,b show global correlation maps between end-of-century TAS changes and the expansion coefficients of *P* change PUPs in the storm-track region. TAS anomalies were pattern-scaled prior to any calculations, in order to minimize the influence of model differences in warming; this was done by dividing each model by its global annual end-of-century TAS change between the 1960–90 and 2070–2100 periods. When this pattern scaling is applied to *P* changes prior to calculating EOFs (not shown), results are similar.

The correlation map for TAS and the first PUP (Fig. 7a) identifies a strong connection between the jet extension and a localized meridional TAS gradient in the middle-to-high-latitude Pacific. For the second mode, the TAS correlations (Fig. 7b) show a connection between the Pacific cold tongue region and storm-track *P* change disagreement.

The tropical correlations in Fig. 7b may suggest that uncertainty in storm-track *P* changes is tied to uncertainty in tropical SSTs via tropical-to-midlatitude teleconnections. Such teleconnections are sometimes referred to as ENSO-like, though we take caution in using this term and define ENSO forcing as a specific SST pattern arising from ocean dynamics in the cold tongue region, as well as deep tropospheric latent heating anomalies in the tropical Pacific that initiate teleconnections (see Zhang et al. 1997). If the uncertainties in SST were truly ENSO-like, one may expect a region of high correlation in tropical *P* changes in the central to eastern Pacific that resemble typical ENSO *P* anomalies. Figures 7c,d show correlation maps between gridpoint *P* changes and the expansion coefficients in Fig. 5. For both modes, the tropical Pacific correlation pattern for *P* is quite different from a canonical ENSO *P* anomaly.

To better quantify the role that intermodel differences in ENSO play in these PUPs, we produce DJF ENSO composite maps for SST and *P* in each model's around 150-yr historical run, project these onto the maps in Fig. 7, and then calculate the correlation between these projection values and the corresponding TAS or *P* change PUP expansion coefficients. This projection method tests whether model differences in the strength and location of historical ENSO SST and *P* anomalies are associated with uncertainties in end-of-century *P* changes in the Pacific storm track. Projections are done for ocean-only grid points between 30°N and 30°S, and ENSO events are defined when the Niño-3.4 index (Trenberth 1997) is more than one standard deviation above (positive) or below
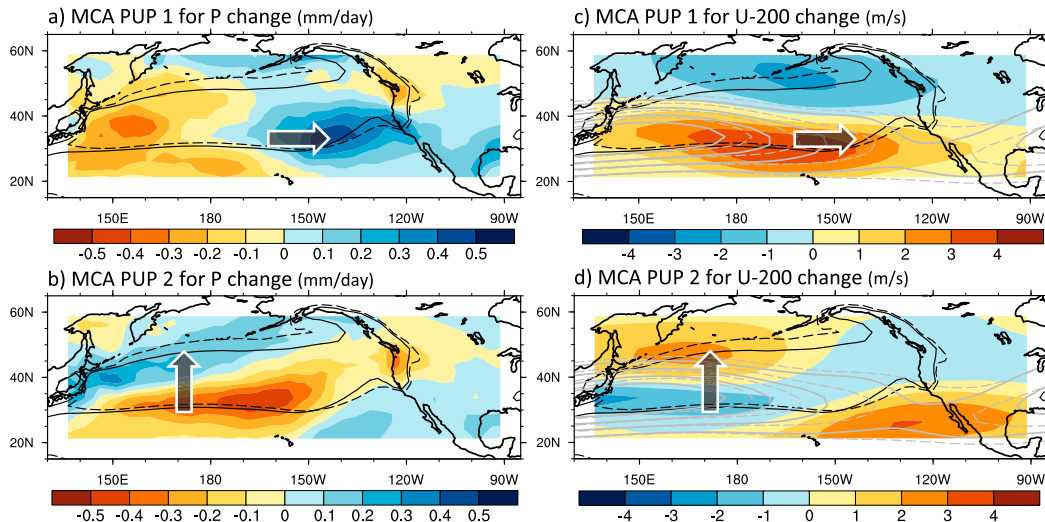
FIG. 6. First and second MCA PUPs showing end-of-century coupled disagreement between DJF (a),(b) *P* and (c),(d) U200 changes. First and second left singular vectors in (a),(b) for *P* (mm day^{-1}). First and second right singular vectors in (c),(d) for U200 change (m s^{-1}). Note the color bar is reversed in (a),(b) vs (c),(d) in order for blue to coincide with positive *P* changes, and red to coincide with positive U200 changes. Schematic arrows are included to depict the jet extension and shift interpretations. The covariance fraction is 31.83% for the first PUP and 23.47% for the second. Black and gray contours are as in Figs. 4e,f.

(negative) the long-term DJF mean. Composites were calculated by extracting linearly detrended *P* and SST fields for ENSO events, averaging positive and negative events separately, and subtracting the two averages (positive minus negative). Correlation values are $r = 0.18$ and 0.18 for the first two correlation maps of TAS (Figs. 7a,b), respectively. Correlation values are $r = 0.15$ and 0.54 for the correlations maps of *P* change PUPs (Figs. 7c,d). These correlation values imply that uncertainties in ENSO composites are able to explain at most about 28% of intermodel uncertainty associated with the two leading PUPs. Correlation values are comparable when SST is substituted for TAS in Figs. 7a,b, and ENSO composites calculated for the RCP8.5 runs give similar results.

We have also defined ENSO-like SST forcing using the first EOF of internal SST variability for each model, which bypasses any requirement that models have correctly placed SST anomalies. These patterns were calculated for detrended DJF SST data between 30°N and 30°S in the historical period. We proceed as above by projecting each model's tropical SST pattern onto Figs. 7a,b and correlate the resulting values with model expansion coefficients. Correlations remain low at $r = 0.20$ and 0.03, and we conclude that *P* change PUPs in the Pacific storm-track region are not primarily a manifestation of ENSO variability among models.

That said, common physical mechanisms will be active in the historical and end-of-century time periods,

and so the uncertainty patterns and modes of internal variability may still resemble another. The extension and shift modes in the storm-track region are similar to those described by Lau (1988), which are related to a "pulsing" and "wobbling" of the Pacific midlatitude jet and have implications in storm development and *P* variability along the North American west coast (e.g., Wettstein and Wallace 2010; Athanasiadis et al. 2010). These jet-driven storm-track fluctuations interact with other modes of circulation variability in the Northern Hemisphere (e.g., Wallace and Gutzler 1981). For instance, the western Pacific (WP) dipole pattern seen in the second mode of U200 change in MCA-based PUPs (Fig. 6d) is similar to the WP pattern investigated by Linkin and Nigam (2008), who identify this as a circulation associated with the North Pacific Oscillation (NPO) and discuss its link to Pacific storm-track fluctuations. Cayan (1992) found that NPO and WP variability at midlatitudes can have broadscale effects on sensible and latent heat fluxes in the Pacific Ocean, affecting tropical SSTs. Complementary studies have discussed the effect of the NPO on sea level pressure anomalies in the midlatitude Pacific, which induce broad SST anomalies that persist into the following summer, affecting trade winds and tropical Pacific climate variability (Vimont et al. 2003; Anderson 2004; Chiang and Vimont 2004). Caballero and Anderson (2009) show that the WP pattern can also influence the strength of the descending branch of the Hadley cell via
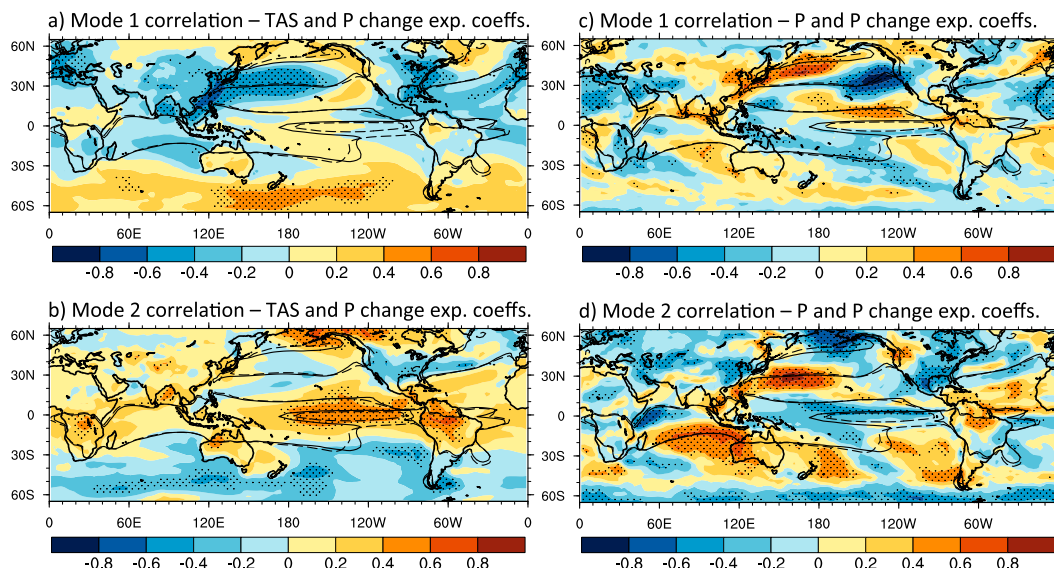
FIG. 7. Correlation maps between expansion coefficients from *P* change PUPs over the storm-track region (in Figs. 4a–d) and either (a),(b) end-of-century model TAS changes across the model ensemble at each grid point, or (c),(d) *P* changes. For (a),(b), TAS anomalies were pattern scaled by the annual end-of-century TAS change (global mean for each model) prior to analysis. Stippling shows where correlations pass a two-tailed Student's *t* test for statistical significance at the 95% confidence level.

stationary wave forcing, which will also affect tropical trade winds and tropical Pacific climate.

It is therefore not out of the question that physical mechanisms underlying *P* change PUPs in the mid-latitude Pacific storm track have qualitative analogs to internal climate variability. However, we contend that the processes giving rise to *P* change PUPs in the storm-track region are to first order distinct from internal climate variability.

7. Patterns of climatological uncertainty and parallels to *P* change PUPs

We also ask whether uncertainties in the base period *P* climatology are related to those for *P* changes. Figures 8a,b show PUPs calculated across model *P* climatology fields during the base period. Shading is for the coupled ensemble (36 members), and blue and red contours depict PUPs for the atmosphere-only ensemble (30 members). These maps represent intermodel uncertainties relative to the MME, and we refer to them as climatology PUPs.

Comparing atmosphere-only (contours) and coupled (shading) PUPs, the disagreement patterns are similar. While there are geographical shifts in emphasis, the first mode (Fig. 8a) depicts an approximate jet extension, along with intermodel spread in the exact latitude that wintertime *P* falls along the North American west coast.

The second mode (Fig. 8b) appears to represent a combination of climatological disagreement over orographic *P* or land–sea contrasts (where the signal is strongest along the coast), as well as a meridional shift over the western Pacific. In general, the enhanced intermodel spread along the North American coast in Figs. 7a,b is not seen in Fig. 4. This implies that similar orographic or land–sea contrast uncertainties are common to both the historical and end-of-century periods and, hence, are not present in differences between the two. As we found previously, this continues to suggest that end-of-century PUPs are depicting intermodel uncertainty in structural changes to climatological patterns, not amplification of those patterns.

To understand how important the coupled ocean is in producing these climatological uncertainties, we calculate PUPs for the 25 coupled models whose atmospheric component is the same in the atmosphere-only runs (see Table S1 in the supplemental material for details). We then project the atmosphere-only climatologies in the storm-track region (centered by the ensemble mean) onto the first two coupled climatological PUPs and correlate these projection values with the coupled expansion coefficients. This allows one to see how much of the overall uncertainty in coupled runs is present in the atmosphere-only runs. Correlation values are $r = 0.65$ and 0.91 for the first two modes, respectively, implying that uncertainty within
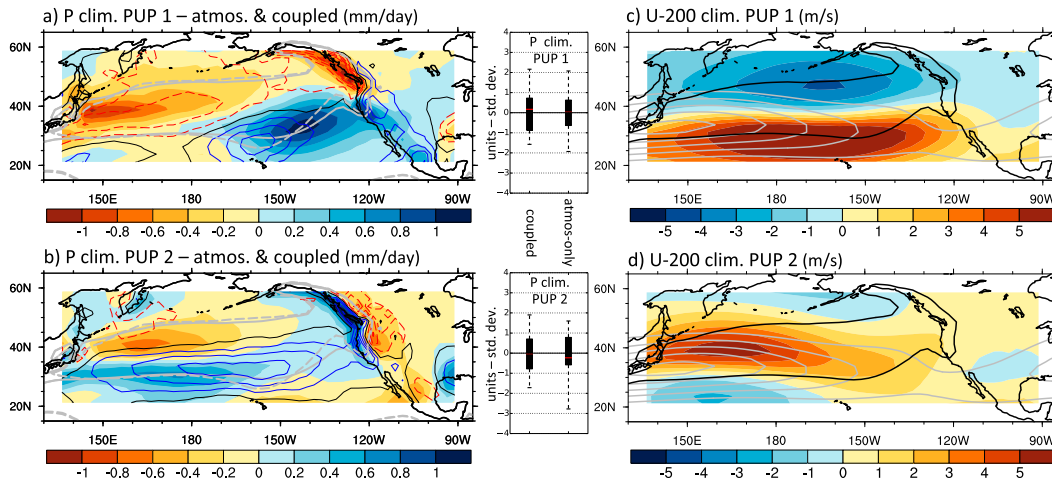
FIG. 8. (a) First and (b) second PUPs for the base period P climatology, in both coupled and atmosphere-only runs. Shaded contours show PUPs for fully coupled historical runs (36-model ensemble, for the period 1960–90), accounting for 26.16% and 16.48% of the variance, respectively. Blue and red contours are overlaid to show PUPs for atmosphere-only runs (30-model ensemble, for the period 1979–2009), accounting for 25.75% and 18.88% of the variance, respectively; contour lines are spaced at an interval of 0.2 mm day^{-1} with the zero contour drawn in black. Box-and-whisker plots to the right of each mode [(a),(b)] show the median (red line), the first and third quartiles (box limits), and the total range (whiskers) of expansion coefficients for the coupled and atmosphere-only runs; units are in standard deviation (i.e., the "typical departure" from the MME mean). (c) First and (d) second EOF PUPs for the base period U200 climatology (atmosphere-only U200 PUPs not shown). The first two modes capture 52.55% and 18.16% of the variance. The color bar is in units of meter per second. End-of-century P and U200 contours are included to show the storm-track outline and the climatlogical jets in the base (solid) and future (dashed) period.

the atmospheric component of the models alone is responsible for a significant amount of the disagreement seen in coupled climatological PUPs.

To quantify whether climatological P uncertainties can predict P change uncertainties among models, we project centered historical climatologies for the 36-model ensemble onto the change PUPs in Figs. 4a–d and then correlate these projections with the corresponding expansion coefficients. The resulting correlations are $r = 0.12$ and 0.47 for the first and second modes, respectively (and cross-mode correlations hover between these values). This implies that within our ensemble, uncertainty patterns in the storm-track P climatology do not serve as strong predictors for the uncertainty seen in the extension mode, though they do have some predictive capacity for the shift mode. When comparing climatological PUPs within the historical and RCP8.5 periods, the relationship is much stronger. Using the same technique by calculating climatology PUPs in the RCP8.5 runs and projecting historical runs onto them, the correlations are $r = 0.89$ and 0.94 for modes one and two, respectively. In other words, there is a strong relationship between intermodel uncertainty in the historical and RCP8.5 climatologies, but when considering the end-of-century differences, the relationship drops significantly. This also supports our earlier point that P change PUPs

represent uncertainty in radiatively forced changes to individual models' climatologies.

Figures 8c,d show PUPs for uncertainties in the U200 climatology. We repeat the analysis above by projecting U200 climatology fields onto the U200 change PUPs from Fig. 4, and we then calculate the correlation between these projection values and the original U200 change PUP expansion coefficients. The correlation values are $r = 0.47$ and 0.42 for the first two modes, respectively, implying that U200 climatological uncertainties can have a modest predictive value for end-of-century change uncertainties. In other words, information about jet shift uncertainty in the historical climatology might provide some information about the jet shift response to radiative forcing, but this does not translate well to information about P change.

We have also explored relationships between U200 PUPs and global P signals for changes and the base period climatology, as well as internal variability in the historical period (see supplemental information for details). We find that there are qualitative similarities among all three cases, especially in the storm-track region, though their global relationships appear to be different, and the correlations patterns are fairly weak. We conclude that storm-track P change uncertainty patterns cannot be explained by any measure of model

differences in internal variability, but are driven primarily by uncertainty in individual model responses to radiative forcing.

8. Summary and conclusions

In this manuscript, we analyze uncertainties in *P* climatologies and end-of-century changes in the CMIP5 ensemble. We borrow objective matrix decomposition techniques from the time series domain to calculate modes of variability across models. This produces spatial patterns of intermodel disagreement in *P* projections, and we refer to them generally as principal uncertainty patterns (PUPs) to emphasize that the relationships they show among fields are of interest independent of the specific method used to calculate them. PUPs are produced using EOF analysis as well as MCA and correlation and/or regression techniques, allowing one to identify leading modes of uncertainty in one field and possible relationships with other fields.

Focusing on a domain encompassing the wintertime midlatitude Pacific storm track, the first *P* change PUP represents intermodel uncertainty in the eastward extension of the steering jet and resulting *P* changes over the North American west coast; this is labeled the "jet extension" mode. The second PUP depicts intermodel disagreement in the extent of a meridional storm-track shift, but this signal is confined to the western Pacific and shows zonal asymmetry farther east; this is labeled the "meridional shift" mode. Regressions of changes in upper- and lower-level winds onto these PUPs reveal uncertainties in circulation that reinforce these interpretations, and MCA analysis provides a check on coupled uncertainty in the zonal wind and *P* fields.

Measures of internal model variability using both additional ensemble members and preindustrial control runs show that internal model variability is not a dominant source of intermodel uncertainty in *P* change PUPs in this region. This is found for both long-term variability and interannual ENSO forcing.

Correlations of TAS changes with the extension and shift PUPs reveal intermodel uncertainties in larger-scale temperature fields associated with Pacific storm-track *P* change PUPs. The first mode shows that uncertainties in changes to meridional temperature gradients are associated with uncertainties in *P* increases at the eastern terminus of the Pacific eddy-driven jet. The second mode shows positive correlations between tropics-wide TAS increases and a poleward storm-track *P* shift in the western Pacific.

In the historical climatologies, *P* and U200 PUPs show patterns that are similar to the extension and shift

modes. While models demonstrate a strong relationship between historical and future climatological uncertainties, these relationships are weak for climatological PUPs and end-of-century change PUPs in the storm-track region. We conclude that the *P* change PUPs in the storm track likely arise from intermodel uncertainty in radiatively forced structural changes to individual model climatologies.

Finally, we reiterate the value of this approach as a set of tools for analyzing patterns of intermodel spread, and we note the applicability of the PUP acronym to any objective process seeking robust uncertainty patterns in an ensemble. Our results highlight the importance of informed domain selection and cross-checking interpretations with complementary procedures. These methods have been used in previous model studies and contribute to the growing body of work in addressing, characterizing, and constraining intermodel uncertainties within an ensemble.

REFERENCES

Allen, M. R., and W. J. Ingram, 2002: Constraints on future changes in climate and the hydrologic cycle. *Nature*, **419**, 224–232, doi:10.1038/nature01092.

Anderson, B. T., 2004: Investigation of a large-scale mode of ocean–atmosphere variability and its relation to tropical Pacific sea surface temperature anomalies. *J. Climate*, **17**, 4089–4098, doi:10.1175/1520-0442(2004)017<4089:IOALMO>2.0.CO;2.

——, B. R. Lintner, B. Langenbrunner, J. D. Neelin, E. Hawkins, and J. Syktus, 2015: Sensitivity of terrestrial precipitation trends to the structural evolution of sea surface temperatures. *Geophys. Res. Lett.*, **42**, 1190–1196, doi:10.1002/2014GL062593.

Athanasiadis, P. J., J. M. Wallace, and J. J. Wettstein, 2010: Patterns of wintertime jet stream variability and their relation to the storm tracks. *J. Atmos. Sci.*, **67**, 1361–1381, doi:10.1175/2009JAS3270.1.

Bengtsson, L., K. I. Hodges, and E. Roeckner, 2006: Storm tracks and climate change. *J. Climate*, **19**, 3518–3543, doi:10.1175/JCLI3815.1.

Berg, N., A. Hall, F. Sun, S. Capps, D. Walton, B. Langenbrunner, and D. Neelin, 2015: Twenty-first-century precipitation

changes over the Los Angeles region. *J. Climate*, **28**, 401–421, doi:10.1175/JCLI-D-14-00316.1.

Brown, J., and Coauthors, 2013: Implications of CMIP3 model biases and uncertainties for climate projections in the western tropical Pacific. *Climatic Change*, **119**, 147–161, doi:10.1007/s10584-012-0603-5.

——, A. Moise, and F. Delage, 2012: Changes in the South Pacific convergence zone in IPCC AR4 future climate projections. *Climate Dyn.*, **39**, 1–19, doi:10.1007/s00382-011-1192-0.

Caballero, R., and B. T. Anderson, 2009: Impact of midlatitude stationary waves on regional Hadley cells and ENSO. *Geophys. Res. Lett.*, **36**, L17704, doi:10.1029/2009GL039668.

Cayan, D. R., 1992: Latent and sensible heat flux anomalies over the northern oceans: Driving the sea surface temperature. *J. Phys. Oceanogr.*, **22**, 859–881, doi:10.1175/1520-0485(1992)022<0859:LASHFA>2.0.CO;2.

Chadwick, R., I. Boutle, and G. Martin, 2013: Spatial patterns of precipitation change in CMIP5: Why the rich do not get richer in the tropics. *J. Climate*, **26**, 3803–3822, doi:10.1175/JCLI-D-12-00543.1.

Chang, E. K. M., 2013: CMIP5 projection of significant reduction in extratropical cyclone activity over North America. *J. Climate*, **26**, 9903–9922, doi:10.1175/JCLI-D-13-00209.1.

——, and M. Zheng, 2013: Medium-range ensemble sensitivity analysis of two extreme Pacific extratropical cyclones. *Mon. Wea. Rev.*, **141**, 211–231, doi:10.1175/MWR-D-11-00304.1.

——, Y. Guo, and X. Xia, 2012: CMIP5 multimodel ensemble projection of storm track change under global warming. *J. Geophys. Res.*, **117**, D23118, doi:10.1029/2012JD018578.

Chiang, J. C. H., and D. J. Vimont, 2004: Analogous Pacific and Atlantic meridional modes of tropical atmosphere–ocean variability. *J. Climate*, **17**, 4143–4158, doi:10.1175/JCLI4953.1.

Chou, C., and J. D. Neelin, 2004: Mechanisms of global warming impacts on regional tropical precipitation. *J. Climate*, **17**, 2688–2701, doi:10.1175/1520-0442(2004)017<2688:MOGWIO>2.0.CO;2.

——, ——, C.-A. Chen, and J.-Y. Tu, 2009: Evaluating the "rich-get-richer" mechanism in tropical precipitation change under global warming. *J. Climate*, **22**, 1982–2005, doi:10.1175/2008JCLI2471.1.

Collins, M., B. B. Booth, B. Bhaskaran, G. Harris, J. Murphy, D. H. Sexton, and M. Webb, 2011: Climate model errors, feedbacks and forcings: A comparison of perturbed physics and multimodel ensembles. *Climate Dyn.*, **36**, 1737–1766, doi:10.1007/s00382-010-0808-0.

Delcambre, S. C., D. J. Lorenz, D. J. Vimont, and J. E. Martin, 2013a: Diagnosing Northern Hemisphere jet portrayal in 17 CMIP3 global climate models: Twentieth-century inter-model variability. *J. Climate*, **26**, 4910–4929, doi:10.1175/JCLI-D-12-00337.1.

——, ——, ——, and ——, 2013b: Diagnosing Northern Hemisphere jet portrayal in 17 CMIP3 global climate models: Twenty-first-century projections. *J. Climate*, **26**, 4930–4946, doi:10.1175/JCLI-D-12-00359.1.

Deser, C., A. Phillips, V. Bourdette, and H. Teng, 2012: Uncertainty in climate change projections: The role of internal variability. *Climate Dyn.*, **38**, 527–546, doi:10.1007/s00382-010-0977-x.

Dettinger, M. D., D. R. Cayan, H. F. Diaz, and D. M. Meko, 1998: North–south precipitation patterns in western North America on interannual-to-decadal timescales. *J. Climate*, **11**, 3095–3111, doi:10.1175/1520-0442(1998)011<3095:NSPPIW>2.0.CO;2.

Durack, P. J., S. E. Wijffels, and R. J. Matear, 2012: Ocean salinities reveal strong global water cycle intensification during 1950 to 2000. *Science*, **336**, 455–458, doi:10.1126/science.1212222.

Flato, G., and Coauthors, 2013: Evaluation of climate models. *Climate Change 2013: The Physical Science Basis*, T. F. Stocker et al., Eds., Cambridge University Press, 741–866.

Giorgi, F., and R. Francisco, 2000: Evaluating uncertainties in the prediction of regional climate change. *Geophys. Res. Lett.*, **27**, 1295–1298, doi:10.1029/1999GL011016.

Greve, P., B. Orlowsky, B. Mueller, J. Sheffield, M. Reichstein, and S. I. Seneviratne, 2014: Global assessment of trends in wetting and drying over land. *Nat. Geosci.*, **7**, 716–721, doi:10.1038/ngeo2247.

Grise, K. M., and L. M. Polvani, 2014: The response of midlatitude jets to increased CO_2: Distinguishing the roles of sea surface temperature and direct radiative forcing. *Geophys. Res. Lett.*, **41**, 6863–6871, doi:10.1002/2014GL061638.

Harr, P. A., D. Anwender, and S. C. Jones, 2008: Predictability associated with the downstream impacts of the extratropical transition of tropical cyclones: Methodology and a case study of Typhoon Nabi (2005). *Mon. Wea. Rev.*, **136**, 3205–3225, doi:10.1175/2008MWR2248.1.

Hawkins, E., and R. Sutton, 2011: The potential to narrow uncertainty in projections of regional precipitation change. *Climate Dyn.*, **37**, 407–418, doi:10.1007/s00382-010-0810-6.

Held, I. M., and B. J. Soden, 2006: Robust responses of the hydrological cycle to global warming. *J. Climate*, **19**, 5686–5699, doi:10.1175/JCLI3990.1.

Hirota, N., and Y. Takayabu, 2013: Reproducibility of precipitation distribution over the tropical oceans in CMIP5 multi-climate models compared to CMIP3. *Climate Dyn.*, **41**, 2909–2920, doi:10.1007/s00382-013-1839-0.

Ihara, C., and Y. Kushnir, 2009: Change of mean midlatitude westerlies in 21st century climate simulations. *Geophys. Res. Lett.*, **36**, L13701, doi:10.1029/2009GL037674.

Jun, M., R. Knutti, and D. W. Nychka, 2008a: Local eigenvalue analysis of CMIP3 climate model errors. *Tellus*, **60A**, 992–1000, doi:10.1111/j.1600-0870.2008.00356.x.

——, ——, and ——, 2008b: Spatial analysis to quantify numerical model bias and dependence: How many climate models are there? *J. Amer. Stat. Assoc.*, **103**, 934–947, doi:10.1198/016214507000001265.

Keller, J. H., S. C. Jones, J. L. Evans, and P. A. Harr, 2011: Characteristics of the TIGGE multimodel ensemble prediction system in representing forecast variability associated with extratropical transition. *Geophys. Res. Lett.*, **38**, L12802, doi:10.1029/2011GL047275.

Knutti, R., and J. Sedláček, 2013: Robustness and uncertainties in the new CMIP5 climate model projections. *Nat. Climate Change*, **3**, 369–373, doi:10.1038/nclimate1716.

——, R. Furrer, C. Tebaldi, J. Cermak, and G. A. Meehl, 2010: Challenges in combining projections from multiple climate models. *J. Climate*, **23**, 2739–2758, doi:10.1175/2009JCLI3361.1.

——, D. Masson, and A. Gettelman, 2013: Climate model genealogy: Generation CMIP5 and how we got there. *Geophys. Res. Lett.*, **40**, 1194–1199, doi:10.1002/grl.50256.

Kumar, S., V. Merwade, J. L. Kinter, and D. Niyogi, 2013: Evaluation of temperature and precipitation trends and long-term persistence in CMIP5 twentieth-century climate simulations. *J. Climate*, **26**, 4168–4185, doi:10.1175/JCLI-D-12-00259.1.

Langford, S., S. Stevenson, and D. Noone, 2014: Analysis of low-frequency precipitation variability in CMIP5 historical

simulations for southwestern North America. *J. Climate*, **27**, 2735–2756, doi:10.1175/JCLI-D-13-00317.1.

Lau, N.-C., 1988: Variability of the observed midlatitude storm tracks in relation to low-frequency changes in the circulation pattern. *J. Atmos. Sci.*, **45**, 2718–2743, doi:10.1175/1520-0469(1988)045<2718:VOTOMS>2.0.CO;2.

Li, G., and S.-P. Xie, 2012: Origins of tropical-wide SST biases in CMIP multi-model ensembles. *Geophys. Res. Lett.*, **39**, L22703, doi:10.1029/2012GL053777.

——, and ——, 2014: Tropical biases in CMIP5 multimodel ensemble: The excessive equatorial Pacific cold tongue and double ITCZ problems. *J. Climate*, **27**, 1765–1780, doi:10.1175/JCLI-D-13-00337.1.

Lin, J.-L., 2007: The double-ITCZ problem in IPCC AR4 coupled GCMs: Ocean–atmosphere feedback analysis. *J. Climate*, **20**, 4497–4525, doi:10.1175/JCLI4272.1.

Linkin, M. E., and S. Nigam, 2008: The North Pacific oscillation–west Pacific teleconnection pattern: Mature-phase structure and winter impacts. *J. Climate*, **21**, 1979–1997, doi:10.1175/2007JCLI2048.1.

Lintner, B. R., M. Biasutti, N. Diffenbaugh, J.-E. Lee, M. Niznik, and K. Findell, 2012: Amplification of wet and dry month occurrence over tropical land regions in response to global warming. *J. Geophys. Res.*, **117**, D11106, doi:10.1029/2012JD017499.

Lu, J., G. A. Vecchi, and T. Reichler, 2007: Expansion of the Hadley cell under global warming. *Geophys. Res. Lett.*, **34**, L06805, doi:10.1029/2006GL028443.

Ma, J., and S.-P. Xie, 2013: Regional patterns of sea surface temperature change: A source of uncertainty in future projections of precipitation and atmospheric circulation. *J. Climate*, **26**, 2482–2501, doi:10.1175/JCLI-D-12-00283.1.

Mahlstein, I., R. W. Portmann, J. S. Daniel, S. Solomon, and R. Knutti, 2012: Perceptible changes in regional precipitation in a future climate. *Geophys. Res. Lett.*, **39**, L05701, doi:10.1029/2011GL050738.

Maloney, E. D., and Coauthors, 2014: North American climate in CMIP5 experiments. Part III: Assessment of twenty-first-century projections. *J. Climate*, **27**, 2230–2270, doi:10.1175/JCLI-D-13-00273.1.

Manabe, S., and R. J. Stouffer, 1980: Sensitivity of a global climate model to an increase of CO_2 concentration in the atmosphere. *J. Geophys. Res.*, **85**, 5529–5554, doi:10.1029/JC085iC10p05529.

——, and R. T. Wetherald, 1980: On the distribution of climate change resulting from an increase in CO_2 content of the atmosphere. *J. Atmos. Sci.*, **37**, 99–118, doi:10.1175/1520-0469(1980)037<0099:OTDOCC>2.0.CO;2.

Mechoso, C. R., and Coauthors, 1995: The seasonal cycle over the tropical Pacific in coupled ocean–atmosphere general circulation models. *Mon. Wea. Rev.*, **123**, 2825–2838, doi:10.1175/1520-0493(1995)123<2825:TSCOTT>2.0.CO;2.

Meehl, G. A., C. Covey, K. E. Taylor, T. Delworth, R. J. Stouffer, M. Latif, B. McAvaney, and J. F. B. Mitchell, 2007: The WCRP CMIP3 multimodel dataset: A new era in climate change research. *Bull. Amer. Meteor. Soc.*, **88**, 1383–1394, doi:10.1175/BAMS-88-9-1383.

Mehran, A., A. AghaKouchak, and T. J. Phillips, 2014: Evaluation of CMIP5 continental precipitation simulations relative to satellite-based gauge-adjusted observations. *J. Geophys. Res. Atmos.*, **119**, 1695–1707, doi:10.1002/2013JD021152.

Neelin, J. D., C. Chou, and H. Su, 2003: Tropical drought regions in global warming and El Niño teleconnections. *Geophys. Res. Lett.*, **30**, 2275, doi:10.1029/2003GL018625.

——, M. Munnich, H. Su, J. E. Meyerson, and C. E. Holloway, 2006: Tropical drying trends in global warming models and observations. *Proc. Natl. Acad. Sci. USA*, **103**, 6110–6115, doi:10.1073/pnas.0601798103.

——, B. Langenbrunner, J. E. Meyerson, A. Hall, and N. Berg, 2013: California winter precipitation change under global warming in the Coupled Model Intercomparison Project phase 5 ensemble. *J. Climate*, **26**, 6238–6256, doi:10.1175/JCLI-D-12-00514.1.

Park, J.-H., and S.-I. An, 2014: Southward displacement of the upper atmosphere zonal jet in the eastern Pacific due to global warming. *Geophys. Res. Lett.*, **41**, 7861–7867, doi:10.1002/2014GL062175.

Roderick, M. L., F. Sun, W. H. Lim, and G. D. Farquhar, 2014: A general framework for understanding the response of the water cycle to global warming over land and ocean. *Hydrol. Earth Syst. Sci.*, **18**, 1575–1589, doi:10.5194/hess-18-1575-2014.

Scheff, J., and D. M. W. Frierson, 2012a: Robust future precipitation declines in CMIP5 largely reflect the poleward expansion of model subtropical dry zones. *Geophys. Res. Lett.*, **39**, L18704, doi:10.1029/2012GL052910.

——, and ——, 2012b: Twenty-first-century multimodel subtropical precipitation declines are mostly midlatitude shifts. *J. Climate*, **25**, 4330–4347, doi:10.1175/JCLI-D-11-00393.1.

Seager, R., and G. A. Vecchi, 2010: Greenhouse warming and the 21st century hydroclimate of southwestern North America. *Proc. Natl. Acad. Sci. USA*, **107**, 21 277–21 282, doi:10.1073/pnas.0910856107.

——, and Coauthors, 2014: Dynamical and thermodynamical causes of large-scale changes in the hydrological cycle over North America in response to global warming. *J. Climate*, **27**, 7921–7948, doi:10.1175/JCLI-D-14-00153.1.

Sheffield, J., and Coauthors, 2013a: North American climate in CMIP5 experiments. Part I: Evaluation of historical simulations of continental and regional climatology. *J. Climate*, **26**, 9209–9245, doi:10.1175/JCLI-D-12-00592.1.

——, and Coauthors, 2013b: North American climate in CMIP5 experiments. Part II: Evaluation of historical simulations of intraseasonal to decadal variability. *J. Climate*, **26**, 9247–9290, doi:10.1175/JCLI-D-12-00593.1.

Shepherd, T. G., 2014: Atmospheric circulation as a source of uncertainty in climate change projections. *Nat. Geosci.*, **7**, 703–708, doi:10.1038/ngeo2253.

Simpson, I. R., T. A. Shaw, and R. Seager, 2014: A diagnosis of the seasonally and longitudinally varying midlatitude circulation response to global warming. *J. Atmos. Sci.*, **71**, 2489–2515, doi:10.1175/JAS-D-13-0325.1.

Taylor, K. E., R. J. Stouffer, and G. A. Meehl, 2012: An overview of CMIP5 and the experiment design. *Bull. Amer. Meteor. Soc.*, **93**, 485–498, doi:10.1175/BAMS-D-11-00094.1.

Tebaldi, C., and R. Knutti, 2007: The use of the multi-model ensemble in probabilistic climate projections. *Philos. Trans. Roy. Soc. London*, **A365**, 2053–2075, doi:10.1098/rsta.2007.2076.

——, J. M. Arblaster, and R. Knutti, 2011: Mapping model agreement on future climate projections. *Geophys. Res. Lett.*, **38**, L23701, doi:10.1029/2011GL049863.

Trenberth, K. E., 1997: The definition of El Niño. *Bull. Amer. Meteor. Soc.*, **78**, 2771–2777, doi:10.1175/1520-0477(1997)078<2771:TDOENO>2.0.CO;2.

——, 2011: Changes in precipitation with climate change. *Climate Res.*, **47**, 123–138, doi:10.3354/cr00953.

Ulbrich, U., J. G. Pinto, H. Kupfer, G. C. Leckebusch, T. Spangehl, and M. Reyers, 2008: Changing Northern Hemisphere storm tracks in an ensemble of IPCC climate change simulations. *J. Climate*, **21**, 1669–1679, doi:10.1175/2007JCLI1992.1.

Vimont, D. J., J. M. Wallace, and D. S. Battisti, 2003: The seasonal footprinting mechanism in the Pacific: Implications for ENSO. *J. Climate*, **16**, 2668–2675, doi:10.1175/1520-0442(2003)016<2668:TSFMIT>2.0.CO;2.

Wallace, J. M., and D. S. Gutzler, 1981: Teleconnections in the geopotential height field during the Northern Hemisphere winter. *Mon. Wea. Rev.*, **109**, 784–812, doi:10.1175/1520-0493(1981)109<0784:TITGHF>2.0.CO;2.

Wettstein, J. J., and J. M. Wallace, 2010: Observed patterns of month-to-month storm-track variability and their relationship to the background flow. *J. Atmos. Sci.*, **67**, 1420–1437, doi:10.1175/2009JAS3194.1.

Yin, J. H., 2005: A consistent poleward shift of the storm tracks in simulations of 21st century climate. *Geophys. Res. Lett.*, **32**, L18701, doi:10.1029/2005GL023684.

Yin, L., R. Fu, E. Shevliakova, and R. Dickinson, 2013: How well can CMIP5 simulate precipitation and its controlling processes over tropical South America? *Climate Dyn.*, **41**, 3127–3142, doi:10.1007/s00382-012-1582-y.

Zhang, C., 2001: Double ITCZs. *J. Geophys. Res.*, **106**, 11 785–11 792, doi:10.1029/2001JD900046.

Zhang, Y., J. M. Wallace, and D. S. Battisti, 1997: ENSO-like interdecadal variability: 1900–93. *J. Climate*, **10**, 1004–1020, doi:10.1175/1520-0442(1997)010<1004:ELIV>2.0.CO;2.

Zheng, M., E. K. M. Chang, and B. Colle, 2013: Ensemble sensitivity tools for assessing extratropical cyclone intensity and track predictability. *Wea. Forecasting*, **28**, 1133–1156, doi:10.1175/WAF-D-12-00132.1.